

*Biochemistry*. Author manuscript: available in PMC 2013 December 21.

Published in final edited form as:

Biochemistry. 2012 December 21; 51(51): 10186–10196. doi:10.1021/bi301279f.

# Conformational Equilibrium of N-Myristoylated cAMP-Dependent Protein Kinase A by Molecular Dynamics Simulations

Alessandro Cembran $^1$ , Larry R. Masterson $^2$ , Christopher L. McClendon $^4$ , Susan S. Taylor $^{4,5,6}$ , Jiali Gao $^{1,3,*}$ , and Gianluigi Veglia $^{1,2,*}$ 

<sup>1</sup>Department of Chemistry, University of Minnesota, Minneapolis, Minnesota 55455, USA

<sup>2</sup>Department of Biochemistry, Molecular Biology, and Biophysics, University of Minnesota, Minnesota 55455, USA

<sup>3</sup>Minnesota Supercomputing Institute, University of Minnesota, Minneapolis, Minnesota 55455, USA

<sup>4</sup>Department of Chemistry and Biochemistry, University of California San Diego, San Diego, California 92093, USA

<sup>5</sup>Department of Pharmacology, University of California San Diego, San Diego, California 92093, USA

<sup>6</sup>Howard Huges Medicinal Institute

#### **Abstract**

The catalytic subunit of protein kinase A (PKA-C) is subject to several post- or co-translational modifications that regulate its activity both spatially and temporally. Among those, Nmyristoylation increases the kinase affinity for membranes and might also be implicated in substrate recognition and allosteric regulation. Here, we investigated the effects of Nmyristoylation on the structure, dynamics, and conformational equilibrium of PKA-C using atomistic molecular dynamics simulations. We found that the myristoyl group inserts into the hydrophobic pocket and leads to a tighter packing of the A-helix against the core of the enzyme. As a result, the A-helix conformational dynamics are reduced and its motions are more coupled with the active site. Our simulations suggest that cation- $\pi$  interactions between W30, R190, and R93 are responsible for coupling these motions. Two major conformations of the myristoylated Nterminus are the most populated: a long loop (LL conformation), similar to PDB:1CMK, and a helix-turn-helix (HTH conformation), similar to PDB:4DFX, which shows stronger coupling between the conformational dynamics observed at the A-helix and active site. The HTH conformation is stabilized by S10 phosphorylation of the kinase via ionic interactions between the protonated amine of K7 and the phosphate group on S10, further enhancing the dynamic coupling to the active site. These results support a role of N-myristoylation in the allosteric regulation of PKA-C.

<sup>\*</sup>Corresponding Author To whom correspondence should be addressed: Dr. Gianluigi Veglia Department of Chemistry and Department of Biochemistry, Molecular Biology, and Biophysics, 231 Church St. SE, Minneapolis, MN 55455. Telephone: (612) 625-0758. Fax: (612) 625-5780. vegli001@umn.edu. Dr. Jiali Gao Department of Chemistry and Supercomputing Institute, University of Minnesota, Minneapolis, Minnesota 55455. Telephone: (612) 625-0769. Fax: (612) 626-7541. gao@jialigao.org..

**Supporting Information**. Predicted N-terminus  $C_{\alpha}$  chemical shifts for the myr(-)p(+) simulation. First 3 principal components, full distance matrices, DCCM and MI analyses for all simulations. This material is available free of charge via the Internet at http://pubs.acs.org.

## Keywords

Protein Kinase A; N-Myristoylation; Phosphorylation; Disorder-to-Order Transition; Molecular Dynamics; Allostery

## 1. Introduction

The cAMP-dependent protein kinase A (PKA) is a prototypical kinase that plays pivotal roles in numerous signaling pathways  $^1$ . PKA exists as a tetramer with two regulatory (R) subunits and two catalytic (C) subunits bound non-covalently  $^2$ ;  $^3$ . Upon  $\beta$ -adrenergic stimulation, cAMP binds the R-subunits and signals the release of the active C-subunits of PKA (PKA-C) that target cellular substrates. PKA-C recognizes and phosphorylates a myriad of substrates  $^{1;4}$ , which carry the canonical recognition sequence RRXSY, where the P-2 and P-3 arginines are followed by a hydrophobic amino acid (X), and the phosphorylation site (S) is flanked by any amino acid (Y)  $^5$ .

PKA-C is a bilobate enzyme, with a small lobe rich in  $\beta$ -strands and a large lobe comprising mostly  $\alpha$ -helices  $^6$  (Figure 1A). The small lobe harbors the nucleotide binding pocket, while the substrate binding cleft is located at the fringe of the large lobe. Catalysis is orchestrated by several flexible regions that activate the enzyme (activation loop), position the substrate (peptide positioning loop), and screen the active site from water (Gly-rich loop), allowing phosphorylation to occur  $^7$ . The motion of these flexible regions is activated upon nucleotide binding  $^{8;\,9}$ , which physically connects the two lobes via the catalytic spine (C-spine)  $^{10}$ .

Recent NMR studies linked the conformational fluctuations of PKA-C with enzymatic turnover, showing that opening and closing of the enzyme is synchronous with  $k_{\rm cat}^{8;\,9}$ . While x-ray studies identified three major conformational states, NMR mapped the average conformational fluctuations of the enzyme, identifying dynamically *committed*, *uncommitted*, and *quenched* states  $^{11}$ . The apo form is dynamically uncommitted, since it does not manifest conformational dynamics synchronous with the turnover; committed dynamics are present in the nucleotide-bound form, while they are quenched in the inhibitor-bound state at high  $Mg^{2+}$  concentration.

PKA-C undergoes several post- and co-translational modifications <sup>7</sup>. Specifically, the highly variable N-terminus can be de amidated <sup>12</sup>, phosphorylated at S10, and myristoylated by N-myristoyl transferase. These modifications are believed to be part of the regulatory system of the kinase <sup>13</sup> and may tune the interactions of the kinase with its binding partners. In particular, the A-helix constitutes the binding site for A-kinase-interacting protein (AKIP), which localizes PKA-C in the nucleus <sup>14</sup>; <sup>15</sup>. In addition, myristoylation increases PKA-C membrane affinity <sup>16</sup>, probably steering the kinase toward membrane bound substrates <sup>13</sup>. PKA-C affinity for the membrane is even more pronounced in the presence of the RII subunit of PKA <sup>16</sup>. Therefore, structural and chemical modifications at the N-terminus might influence the binding affinity for different partners.

N-myristoylation is one of the least studied aspects of PKA-C, due to difficulties in obtaining homogenous myristoylation in recombinant expression systems. We recently overcame this problem using an *in vitro* myristoylation protocol that enables the production of isotopically labeled protein in quantities sufficient for NMR studies <sup>17</sup>. Both myristoylation and membrane binding of PKA-C induce allosteric effects in the enzyme, including regions at the active site <sup>17</sup>. Based on chemical shift trajectories, we also hypothesized two conformational states undergoing fast equilibrium on the NMR time scale: a *myr-in* state, where the acyl group is tucked into the core of the enzyme, and a *myr-out* 

state, where the acyl group is partially or completely extruded. Along the path of these two major states, we identified two additional states that reflect folding/unfolding of the N-terminal helix. Thus, the extrusion of the acyl group – which is catalyzed by the presence of lipid membrane – is also accompanied by a folding/unfolding equilibrium. This equilibrium is affected by phosphorylation at S10 <sup>17</sup>, forming a so-called myristoyl/phosphoserine switch <sup>13</sup>. Furthermore, in a recent study Taylor and co-workers used a myristoylated PKA-C mutant (K7C, lacking phosphorylation at S10), which demonstrated a marginal increase in catalytic rate <sup>18</sup>. On the basis of X-ray data, they proposed that the observed rate enhancements were due to long-range effects of the mutation/phosphorylation on the opening and closing of the active site, affecting the rate-limiting step of the enzyme (V-type allostery).

In this article, we test these hypotheses, analyzing the effects of N-myristoylation on the conformational equilibrium of PKA-C using atomistic molecular dynamics simulations. In the absence of myristoylation, we found that the N-terminal A-helix is among the most dynamic regions of the enzyme, while N-myristoylation caps the A-helix and induces a more compact conformation of the enzyme that shields the hydrophobic pocket from water molecules. In this form, the conformational dynamics of the A-helix are substantially reduced and strongly coupled to the core of the protein. In addition, we identified cation- $\pi$ interactions between W30, R190, and R93 that are responsible for transmitting motions from the A-helix to the active site, consistent with previous studies highlighting the importance of these residues <sup>19; 20</sup>. The myristoylated N-terminus adopts two stable conformations: one characterized by a long loop (LL), resembling the X-ray structure of the myristoylated Csubunit (PDB:1CMK) <sup>21</sup>, and a helix-turn-helix (HTH) conformation similar to that was recently crystallized(PDB:4DFX) <sup>18</sup> with a deeper insertion of the myristoyl group in the hydrophobic pocket. This conformation is further stabilized by S10 phosphorylation and displays a stronger coupling between the A-helix and active site motions. The occurrence of these conformations at the N-terminus is coupled with a rearrangement of the active site, which may explain the increased catalytic rates observed in the K7C mutant <sup>18</sup>.

## 2. Materials and Methods

#### **System Setup**

The crystal structure of PKA-C in the closed conformation (PDB: 1ATP  $^{22}$ ) was used as the main template for setting up all of the simulations. The myristoyl group and the first 19 residues of the A-helix were built from the N-myristoylated crystal structure (PDB: 1CMK  $^{21}$ ) after alignment of the large lobe with 1ATP. We will refer to this hybrid structure as 1ATP\*. In all simulated systems, T197 and S338 were phosphorylated with fully ionized phosphate groups. The protonation state of the histidine residues 62, 68, and 260 was set to neutral with a proton on the N8; histidines 131, 142, 158, and 294 were set to neutral with a proton on the Ne. H87 was considered to be protonated, as it can form a hydrogen bond with both the phosphate group of T197 and the side-chain of Q84  $^{23}$ . Overall, the charge of the nucleotide-bound kinase ranged between 0 and  $^{-2}$ , depending on the myristoylation and phosphorylation states.

We set up a total of 5 simulation systems, all starting from the same closed conformation 1ATP\*. Four systems were in the binary form, with ADP and one  $Mg^{2+}$  ion bound to mimic low-magnesium concentrations  $^{24}$ . These systems differed by the presence or absence of N-myristoylation, myr(+) and myr(-), respectively, and phosphorylation at S10, p(+) and p(-), respectively. To determine the effects of myristoylation and phosphorylation, we carried out four different simulations: one for myr(+)p(+), one for myr(-)p(+), and two for myr(+)p(-). From the analysis of the simulations, we found that the simulations of the myr(+) enzyme converged into two different conformations at the N-terminus: the first conformation

characterized by a long loop (LL) and the second by a helix-turn-helix (HTH) motif. Specifically, the myr(+)p(+) form of the enzyme adopted the HTH conformation, while the myr(+)p(-) form sampled both the LL and HTH conformations. To mimic the dynamically quenched state of the enzyme <sup>11</sup>, we simulated a myr(+)p(+) form in complex with PKI<sub>5-25</sub>, ATP and two Mg<sup>2+</sup> ions <sup>25</sup>. All of the simulation systems were solvated in a cubic box with a side length of 90.5 Å, consisting of about 23,000 water molecules modeled by the TIP3P model <sup>26</sup>. The positions of crystal waters were retained, and depending on the system, 60-61 chloride and 60-62 potassium ions were added to ensure electrostatic neutrality and an ionic strength of approximately 150 mM. The CHARMM22 force field <sup>27</sup> with CMAP correction <sup>28</sup> was used for the protein, while the parameter files CHARMM27 <sup>29</sup> and CHARMM36 30 were employed for the nucleotides and myristoyl group, respectively. All of the simulations were set up using CHARMM <sup>31</sup> c36a5 <sup>32</sup> and molecular dynamics were performed with NAMD 2.7 33. The RATTLE algorithm was applied to all bonds involving hydrogen <sup>34</sup>, and dynamics were propagated with the r-RESPA <sup>35</sup> integrator with time steps of 1 fs and 4 fs for short and long range interactions, respectively. Van der Waals forces were truncated with a switching function between 11 and 12 Å. Particle mesh Ewald <sup>36</sup> was used for electrostatic interactions with a real space cutoff of 12 Å, a  $\kappa$  of 0.26 Å<sup>-1</sup>, and a grid of approximately 1 Å. The temperature was controlled by Langevin dynamics using a damping constant of 1.0 ps $^{-1}$ , and the Nosé-Hoover method  $^{37}$  was used for the constant pressure simulations.

After initial minimization, the system was gradually heated from 50 K to 300 K over 10 ns at constant volume, with harmonic restraints on the heavy atoms of the protein and nucleotide with a force constant of 100 kcal/(mol  $\mathring{A}^2$ ). The restraints were gradually released (side-chain first, then backbone) over 10 ns of constant pressure (1 atm) and temperature (300 K) MD. The systems were then fully equilibrated for additional 20 ns without restraints before data were collected for analysis every 5 ps. Each system was simulated for approximately 230 ns, resulting in a total simulation time of more than 1  $\mu$ s.

#### Principal component analysis (PCA)

To identify large-scale, low-frequency motions of the systems, we computed their Cartesian principal components <sup>38</sup> using the Bio3D package <sup>39</sup>. We aligned the trajectories using the E (residues 140-160) and F (217-233) helices <sup>11</sup>, and carried out PCA for all the backbone atoms and the heavy atoms of the myristoyl group, analyzing each trajectory individually. To compare the motions for the various species, we also pooled several trajectories together and performed PCA on the resulting ensemble. The opening and closing modes of the Glyrich loop and the entire enzyme were probed with PCA on residues 50-300 using the combined trajectory from all of simulations.

The first principal component (PC1) corresponds to the opening and closing motions of PKA, while the correlation of the S53-G186 distance tracks the Gly-rich loop motion <sup>11</sup>. To relate the distribution along these components with the crystal structures used in the set up, we projected the coordinates of 1ATP\* and 1CMK along these components. As 1ATP\* and 1CMK are in closed and open conformation, respectively, this projection also provides a reference for the opening and closing of the active site cleft.

#### Root mean square fluctuations (RMSF)

To describe the motions of the protein backbone, we analyzed the RMSF of the amide nitrogen atoms. To relate our results with the fast conformational dynamics captured by NMR experiments  $^{11}$ , we focused on the fluctuations taking place in the sub-nanosecond time scale. For residue i, the picosecond-to-nanosecond RMSF is defined as:

RMSF (i) = 
$$\left\langle \frac{1}{T} \sum_{t=0}^{T=1ns} \sqrt{\sum_{q=x,y,z} (q_i(t) - \overline{q}_i)^2} \right\rangle_{trj}$$

in which the Cartesian coordinate  $\overline{q}_i$  is averaged over T=1 ns windows, and the brackets represent averaging of these windows over the entire trajectory following alignment with the crystal structure.

#### Distance matrix analysis

For all of the systems, we computed the distance matrix between  $C_{\alpha}$  and myristoyl group carbon atoms on structures saved every 5 ps during the simulations and averaged the results over the entire trajectories. The difference plots of the distance matrices were used to probe the changes between the various conformations.

# **Dynamical cross-correlation matrix (DCCM)**

We used cross-correlation maps to identify regions with correlated and anti-correlated motions. We first aligned the snapshots from the trajectories using the most rigid elements of the kinase (residues 140-160 and 217-233), and then computed the correlation coefficient matrix, whose elements are defined as:

$$C_{ij} = \frac{\left\langle (r_i - \langle r_i \rangle) \left( r_j - \left\langle r_j \right\rangle \right) \right\rangle}{\sqrt{\left( \left\langle r_i^2 \right\rangle - \left\langle r_j \right\rangle^2 \right) \left( \left\langle r_i^2 \right\rangle - \left\langle r_j \right\rangle^2 \right)}}$$

in which the  $r_i$  is the positional vector of the  $C_{\alpha}$  of residue i or myristoyl carbons. Averages were computed over 50 ns windows, and the resulting C matrices averaged over the full trajectories along 25 ns sliding windows. With this procedure, it is possible to associate the standard deviations with computed correlations; these can then be used with error combination rules for comparing the different systems. To identify significant correlation

changes between  $(C_{ij}^A - C_{ij}^B)$  of two different systems, we considered only correlation differences larger than two standard deviations, and absolute values of the correlations  $(C_{ij})$  greater than 0.2 units of correlation. The first rule was set to discard changes in correlation with confidence less than 95%, the second to discard changes affecting residues characterized by low correlation.

In addition to the positional vector correlation matrix analysis, we used torsion angle correlation analysis of the  $\phi/\psi$  angles of the kinase backbone and all angles of the myristoyl group. The basic principles follow the spatial DCCM analysis described above, with two differences: (a) each dihedral is centered around its average and wrapped, and (b) the Pearson correlation coefficient is computed in the sine domain  $^{40;\,41}$ . The trajectories were analyzed using the same protocol for the DCCM analysis, with identical thresholds for standard deviation and absolute value of correlation.

## MutInf analysis

We also applied the MutInf method  $^{42}$  to identify clusters of residues with highly correlated motions, according to their backbone and side chain  $\phi/\psi/\chi$  torsion angles. We calculated the mutual information (MI) between pairs of torsion angles using adaptive partitioning with 12 bins per degree of freedom. The excess MI for each pair of torsion angles was filtered as

reported in  $^{42}.$  To determine the requisite sampling bias term, we split each simulation into two halves and calculated the bias term as the MI between torsion angles in different halves of the simulation. We then took the excess MI for each pair of torsion angles and subtracted the bias term. We calculated the MI between each pair of residues summing over all  $\phi/\psi/\chi$  torsions pairs according to the MI expansion  $^{43}.$  We then hierarchically clustered the matrix of residues' MI values using a Euclidean distance metric. With this approach, residues characterized by similar MI patterns are clustered together as previously reported  $^{42;\,44;\,45}.$ 

## 3. Results

In our simulations, we analyzed the local and long-range changes of conformational dynamics occurring at the N-terminus upon-myristoylation and S10 phosphorylation. Important regions and amino acids discussed in the text are highlighted in Figure 1A-B, the distance matrix in Figure 1C identifies regions that are spatially close. Regions at close distance with the myristoyl or the A-helix are shown with thick red ribbons in Figure 1A.

## The motions at the N-terminus are quenched upon N-myristoylation

The MD simulations for myr(–) PKA-C show that the N-terminal region of the A helix (up to residue 14) is very flexible and samples a variety of conformational states, in agreement with both nuclear spin relaxation data <sup>8; 10; 11</sup>, NMR chemical shift indices <sup>46</sup> and X-ray diffraction data <sup>10</sup>. An overlay of 33 different snapshots taken every 25 ns from the MD trajectory is reported in Figure 2A and shows the conformational spread. While we did not observe a complete unfolding of residues 1-14 for the myr(–)p(+) PKA-C in the time scale of the MD simulations, as predicted by crystallographic and NMR data (Figure S1), we did observe complete unfolding of residues 1-7. PCA performed on the trajectory (Figure 2B) shows that the largest components, in addition to the opening and closing of the enzyme, describe a 'pendulum like' motion of the A-helix in planes that are parallel and perpendicular to the protein surface, thus globally sampling a conical space.

The magnitude of the A-helix motions is greater than the opening and closing modes. In fact the terminal part of A-helix undergoes substantial conformational dynamics and is structurally disconnected from the hydrophobic pocket. Upon N-myristoylation, the conformational dynamics of the N-terminus are attenuated, but not completely quenched (Figure 2A). Increased ordering at the N-terminus of myr(+)PKA-C is in qualitative agreement with the increased thermal stability of the N-myristoylated enzyme <sup>17; 47</sup>. While still sampling different conformations, the initial part of the N-myristoylated A-helix has more restricted motions and remains more closely packed against the protein surface. Additionally, all the N-myristoylated binary complexes retain both opening/closing and shearing motions <sup>11</sup>. In contrast, the conformational dynamics at the N-terminus are described by different modes and are substantially attenuated with respect to the unmyristoylated enzyme (Figure 2B).

The sub-nanosecond dynamics of the A-helix are also affected by N-myristoylation, as evidenced by the RMSF analysis in Figure 2C-D. In fact, the first 14 residues of the A-helix are more flexible in the absence of myristoylation. In contrast, the other residues in the A-helix and those in the rest of the protein do not show substantial changes in backbone amide dynamics. These results are in agreement with the poor electron density observed for residues 1-14 in the X-ray structures of myr(–)PKA-C<sup>48</sup>.

# The myr-in/myr-out transition is coupled with folding/unfolding at the N-terminus

Using NMR and fluorescence spectroscopy in concert with crystallographic data, we concluded that myr(+) PKA-C <sup>47</sup> undergoes conformational equilibrium between *myr-in* and

*myr-out* states <sup>17</sup>, which are characterized by different conformations at the N-terminus. In the *myr-in* state, the myristoyl group is retracted into the hydrophobic pocket and the A-helix is in an ordered helical conformation. In contrast, the A-helix in the *myr-out* state is more disordered and the N-terminus exposed to the bulk solvent. We also identified intermediate states reflecting folding/unfolding of the N-terminus and proposed that local unfolding is an integral part of the extrusion of the myristoyl group from the hydrophobic pocket of the enzyme.

MD simulations identified two basins for the *myr-in* state characterized by two different N-terminus conformations along the folding/unfolding equilibrium, supporting the correlation between the myr-in/myr-out equilibrium and the folding/unfolding process of the N-terminal region of the A-helix. In fact, the PCA reported in Figure 3A reveals that this correlation occurs during the two myr(+)p(-) simulations. Specifically, PC1 captures the folding/ unfolding motion of the N-terminal region of the A-helix coupled with a partial extrusion of the myristoyl group from the hydrophobic pocket (PC1 in Figure 3A, transition from blue to red). PC1 separates the trajectories in two well-defined basins corresponding to the HTH and LL conformations, while PC2 – tracking smaller and global changes – shows a uniform distribution of the conformations. Representative snapshots from the LL and HTH conformations are reported in Figure 3B, which highlights that the LL to HTH transition involves a rotation around K7 backbone dihedral angles. These observations agree well with the NMR data, which showed a linear progression between folded (myr-in) and unfolded (myr-out) forms.

We also performed a high-temperature simulation on a myristoylated ternary complex, starting with the N-terminus in the HTH conformation. The bath temperature was increased from 300 K to 500 K over a period of 20 ns and the simulation was then continued for a total of ~70 ns, enabling the sampling of a greater conformational space than low temperature simulations. Under these conditions, the enzyme maintains its original fold, with the exception of the N-terminal residues 1-7, which unfold during the simulations at high temperature (see Figure 3C). This simulation resulted in the progressive extrusion of the myristoyl group from the hydrophobic pocket, suggesting its propensity to switch into the *myr-out* state. The activation barrier for this transition is relatively low in the presence of membranes, but it becomes higher the absence of membranes <sup>17</sup>. Taken together, the above results agree well with the linear trend of NMR chemical shifts observed experimentally, and support the metamorphic nature of this region in PKA-C.

#### Phosphorylation reduces the conformational dynamics at the N-terminus

Upon phosphorylation at S10, the myr(+) enzyme trajectories sampled mostly the HTH conformation with the myristic group embedded in its binding groove. This finding is illustrated by the PCA analyses of phosphorylated and un-phosphorylated trajectories pooled together (Figure 3A), which showed that S10 phosphorylation restricts the conformational space explored by the enzyme to a smaller subspace. To test whether this was an artifact of the starting conditions, we set up a new simulation for the myr(+)p(+) enzyme, which produced similar results (see myr(+)p(+)trj(2) in Figure 3A). Throughout all simulations, we observed persistent electrostatic interactions between the phosphate group of phosphoserine-10 and the side chain of K7 (see Figure 4B and 4D); these interactions were responsible for the limited conformational freedom of the phosphorylated isoform. In fact, the ionic bond hinders rotation of the K7 dihedral angles and restricts the conformational space accessible to the N-terminal residues of the A-helix. However, these interactions are absent in both simulations with the unphosphorylated forms of the enzyme (Figure 4B and 4D). The latter resulted in a lower barrier for the LL/HTH transition, which then allows sampling of a larger conformational space. The stabilization of the HTH motif upon S10 phoshorylation is likely to be correlated to the chemical shift perturbations observed for the

N-terminal residues of PKA-C <sup>17</sup>. Interestingly, the K7C mutation has a similar effect on the un phosphorylated isoform 18, further suggesting that the LL/HTH conformational equilibrium is sensitive to changes in the charge distribution of this region, particularly to positions 7 and 10.

## Allosteric coupling between the N-terminus/A-helix and catalytically-relevant regions

Long-range perturbations observed via chemical shift mapping suggested an allosteric communication between the N-terminal myristic group and regions surrounding the ATP binding pocket  $^{17}$ . These effects were observed experimentally upon-myristoylation, S10 phosphorylation, and/or membrane interaction. In this work, we compared different MD simulations to map short- and long-range effects arising arising at the N-terminus: a) myristoylation from the myr(+)p(+) vs. myr(-)p(+) comparison; b) LL/HTH conformational change from myr(+)p(-)LL vs. myr(+)p(-)HTH; and c) S10 phosphorylation from myr(+)p(+) vs. myr(+)p(-)HTH. We analyzed the trajectories with distance matrix, Cartesian DCCM, torsion angle correlation matrix, and mutual information. The first two methods emphasize global spatial perturbations, while the other two perform better in identifying hinges and flexible regions responsible for those changes. In Figure 4 we mapped the DCCM differences on the PKA-C residues, color-coding the correlations identified with the three different methods (see Material and Methods).

All three perturbations at the N-terminus resulted in both short- and long-range effects (Figure 4). Overall, increased dynamic correlations involving the A-helix and regions involved in catalysis were observed upon N-myristoylation, conformational change from LL to HTH, and S10 phosphorylation. Common to all perturbations are the increased dynamic correlations involving the C-terminus of the A-helix (residues 25-35), residues in β-strand 9 (~189-191), and the C-terminus of the C-helix, which together form an allosteric node for signal transmission (see Figure 1A). The importance of the A-helix was emphasized by Xray crystallographic studies, which suggested its role in anchoring the small to the large lobe <sup>7; 19</sup>, also tethering the C-terminus end of the conserved C-helix, a critical region for all protein kinases <sup>7</sup>. Noticeably, the turn of the C-helix including residues 91-93 was proposed to be an important signal integration motif interacting directly with the active site, the Nterminus, and the C-terminus <sup>7</sup>. On the other end, the increased dynamic correlations between residues in the A-helix with those in β-strand 9 are also important, since β-strand 9 is situated between the Mg<sup>2+</sup>-positioning loop and the activation loop, both critical elements for catalysis. According to previous X-ray studies <sup>7</sup>; <sup>18</sup>, the R190 side chain of β-strand 9 is involved in cation- $\pi$  interactions with the aromatic rings of both F26 and W30, which bridge the active site to the A-helix. The structures also indicate that the W30/R93 interaction helps to anchor the N-terminal A-helix. Remarkably, we found that these interactions are persistent throughout all of the simulations as indicated by the center of mass distance between the guanidinium group of the arginine and the aromatic rings (Figure 5). Notice that standard force fields underestimate the strength of cation- $\pi$  interactions  $^{4951}$  For the F/R pair, we calculated that CHARMM underestimates the binding energy between the aromatic and guanidinium moieties in gas phase by 3.7 kcal/mol with respect to the value computed at the BSSE-corrected MP2/aug-cc-pVDZ level (14.4 kcal/mol). The other interactions between the A-helix and the protein core are mainly hydrophobic, as shown in Figure 6, and form a "hydrophobic joint", which provides flexibility to this region and facilitates the shearing motions between the two moieties <sup>19</sup>. Figure 6 also shows that the myristoyl group displaces the water from the hydrophobic pocket and finds its position directly below the hydrophobic joint, in close contact with the C-terminus of the C-helix (see also Figure 1), thus contributing to the packing of the A-helix against the protein core. We relate the changes in dynamic correlations described above to the higher degree of structural coupling between the A-helix and the protein core upon-myristoylation. In fact, the more tightly-

packed N-terminus HTH conformation displays higher dynamic correlations than the partially extruded LL conformation, and stabilization of the HTH conformation upon S10 phosphorylation further enhances these structural and dynamical correlations. Remarkably, there is a clear trend between the packing of the A-helix to the core of PKA-C and the extent of the correlated motions observed for the C-terminal residues of the A-helix,  $\beta$ -strand 9, and the C-terminal of the C-helix; proper positioning of the C-helix is critical for the formation of the regulatory spine common to all active kinase structures  $^{10;\,52}$ .

The cluster of residues involved in the allosteric node (A-helix/ $\beta$ -strand 9/C-helix) is probably responsible for the propagation of motions to other remote regions of the kinase, although the number of residues affected varies among the different forms of the enzyme. Indeed, N-myristoylation has the largest effect, followed by S10 phosphorylation and LL to HTH conformational change. We found that upon-myristoylation (Figure 4A) a large section of the small lobe displays increased correlated motions with C-terminal residues of the A-helix and Mg<sup>2+</sup>-positioning and catalytic loops. In particular, the Gly-rich loop,  $\beta$  strands 3 and 6, the B-helix and the acidic patch are directly involved. These regions play a major role in catalysis. Some of these regions overlap with those observed experimentally through chemical shift perturbations <sup>17</sup>. In particular, both approaches showed that perturbations affected the allosteric link, the Gly-rich loop, and the acidic patch. Also, both identified the conserved K72, which anchors the phosphates of the nucleotide and tracks the kinase opening/closing mode <sup>11</sup>, and V104, which is van der Waals contact with the adenine ring of the nucleotide.

PCA (Figure 7) and distance matrix analyses (Figure S3A-B in the Supporting Information) also help identify global changes. PCA (Figure 7B) shows that the myristoylated form samples slightly more closed conformations both along the global opening/closing mode (PC1) and along the Gly-rich loop opening/closing mode (S53-G186 distance). However, the conformational space sampled is still between the open and intermediate conformations, as expected for a binary complex (see the position of 1CMK in Figure 7B). Nevertheless, it is possible that the enhanced correlations observed in the small lobe/active site upon-myristoylation could be traced back to a more compact structure that enhances structural and dynamic couplings between these regions.

The effects of the conformational transition from LL to HTH are smaller than those observed upon-myristoylation and localized in the A-helix/allosteric node. Nevertheless, in the HTH conformation increased correlations are observed between the N-terminus and the J-helix (see Figure 4B), which can be related to the closer packing of the first 7 residues against the J-helix in this conformation. This observation agrees well with experimental data, which shows that W302 (located in the J-helix) is sensitive to changes occurring in the hydrophobic pocket <sup>11</sup>. Noticeably, W302 is also sensitive to active site occupancy <sup>11</sup>. To this end, we also notice that occurrence of the HTH conformation is accompanied by an opening of the Gly-rich and peptide positioning loops of approximately 3 Å (Figure 7C and Figures S3C-D). This is in remarkable agreement with recent X-ray structures with conformations at the N-terminus similar to the HTH <sup>18</sup>.

Finally, we found that the HTH conformation is more stable upon S10 phosphorylation, packing the A-helix to the core of the enzyme (see Figure 4C). The regions affected by increased correlations are similar to those observed upon-myristoylation, although they involve fewer residues. This agrees well with chemical shift perturbation results <sup>13</sup> which show that S10 phosphorylation has a smaller effect than N-myristoylation. We propose the existence of a preferential allosteric pathway across the enzyme that connects the N-terminus to the active site as the changes observed in the A-helix result in a slightly more closed state of the enzyme (see Figure 7C).

# 4. Discussion

A complete description of enzymatic activity requires characterization of the most populated structural basins in the free energy landscape, as well as the fluctuations around these basins, *i.e.*, conformational dynamics <sup>53</sup>. These structural fluctuations often accompany large-scale reorganization of structural domains as well as atomic fluctuations around highly-populated conformations. Recent reports have emphasized the importance of both phenomena <sup>54-64</sup>, and limiting cases in which motions rather than conformational changes drive the enzymatic function have also been hypothesized 65; 66. In its enzymatic cycle, PKA-C displays substantial conformational changes in those structural domains directly involved in catalysis, as well as dynamic changes that extend throughout the enzyme backbone. Using NMR spectroscopy in concert with X-ray data, we identified three major states (open, intermediate, and closed) with different structural dynamics <sup>8; 11</sup>. Our previous studies mapped all of these states and showed that the pre existing equilibrium encoded in the apo form is shifted by addition of the ligands (nucleotide and substrate) <sup>8; 11</sup>. In the dynamically committed state (nucleotide bound), the enzyme's conformational dynamics in the μs-ms time scale are enhanced to allow substrate recognition as well as product release.

Based on chemical shift perturbations observed in our previous work, we proposed that the conformational equilibrium of PKA-C can be modulated by myristoylation or by S10 phosphorylation <sup>17</sup>. The current study rationalizes these effects by defining the conformational landscape of the kinase in the presence of the myristoyl/phosphoserine switch. Not only does the myristoyl/phosphoserine switch act on the membrane affinity of the kinase, it also shifts the conformations of the kinase to states with altered structure and dynamics <sup>16</sup>; for example, the addition of the myristoyl group at the N-terminus causes an overall compaction of the enzyme and increases thermostability <sup>47</sup>. In the absence of myristoylation, the A-helix is partially unfolded, which facilitates the entrance of water in the hydrophobic pocket (Figure 6), and as a result, the A-helix undergoes a pendulum-like motion (Figures 2B), which is facilitated by its greasy interface between the hydrophobic joint and the core of the enzyme (Figure 6). Once myristoylated, the N-terminal residues fold back towards the enzyme's core, excluding water and partially quenching the conformational dynamics of the N-terminus. Phosphorylation of S10 further shifts the equilibrium towards the more compact conformation via formation of a stable ionic bond between the phosphate and the side-chain of K7, a conformation which closely resembles the recently identified X-ray crystal structure of the N-myristovlated PKA-CK7C mutant 18. In both the crystallographic and the simulated structures the helix is broken at K7, which then displays dihedral angles typical of a \beta-sheet conformation. These results are in good agreement with NMR and X-ray experiments and provide a rationale for the observed higher thermal stability of the myristoylated isoform.

We also investigated whether the effects of N-myristoylation are propagated in remote areas of the enzyme. In fact, our NMR chemical shift perturbation data show that myristoylation affects residues at the active site, the acidic patch as well as the C-helix, suggesting that myristoylation could act as an allosteric modulator of the kinase function. Analyses of interatomic distance patterns and correlated motions from MD simulations support this hypothesis. Our atomistic simulations trace structural and dynamic changes involving the N-terminus and A-helix that are correlated with the active site residues. Specifically, perturbations caused by myristoylation, S10-phosphorylation, and/or conformational changes occurring at the N-terminus are propagated to the C-terminal residues of the A-helix, from where they are re routed to the C-helix and  $\beta$ -strand 9 through the *allosteric node* (see Figure 1A) formed by the aromatic residues F26-W30 <sup>19</sup> and arginines R94-R190, as inferred by X-ray data <sup>18</sup>. The *hydrophobic joint* is part of the *allosteric node*, which is an essential element for effective transmission of the allosteric signals. While the cation- $\pi$ 

interactions couple intermolecular motions between the A-helix and the core of the enzyme, the flexibility of the hydrophobic joint allows these motions to take place. The majority of the perturbations are localized at the interface between the two lobes (shaded area in Figure 1A), forming a contiguous path connecting the A-helix to the nucleotide and active site, although other non-contiguous perturbations are also observed.

Our analyses reveal a clear trend of the structural dynamic correlations among the different forms of the enzyme. Going from the unmyristoylated to myristoylated and S10 phosphorylated forms of the enzyme, there is a tighter packing of the A-helix against the kinase core with an increased number of structural and dynamic correlations (Figure 8).

The HTH conformation stabilized by phosphorylation has the highest number of structural dynamic correlations and is similar to the X-ray structure of the PKA-C<sup>K7C</sup> mutant <sup>18</sup>. Upon-myristoylation, this mutant is characterized by a two-fold increase of  $k_{cat}$  and, unlike the wild-type, retains the HTH conformation in the ternary complex. Therefore, we hypothesize that the increased catalytic rate constant observed in the myristoylated mutant might be due to the HTH conformation that is able to affect the active site residues allosterically (V-type allostery). Interestingly, detergents such as MEGA-8 mimic the effect of myristoylation on the chemical shifts <sup>17; 67</sup>. Therefore, it might be possible that 'myrpocket binders' that stabilize the HTH conformation can be used to modulate PKA-C activity in a manner similar to Abl kinase <sup>68</sup> and represent drug candidate alternatives to ATP-site directed inhibitors.

In summary, we have mapped the effects of myristoylation and S10 phosphorylation on the conformational equilibrium of PKA-C in the absence of a membrane mimetic environment. We showed that both events drive the kinase equilibrium toward different conformational states that could be relevant for the interaction and regulation of the C-subunit in the presence of the regulatory subunits. These studies also suggest that myr-directed drugs can be, in principle, designed to target the PKA-C in a manner analogous to Abl kinase, circumventing the non-specificity of ATP-directed inhibitors.

# **Supplementary Material**

Refer to Web version on PubMed Central for supplementary material.

# Acknowledgments

This work is supported by the National Institutes of Health to G.V (GM100310) and J.G. (GM46736).

## **ABBREVIATIONS**

**PKA-C** protein kinase A catalytic subunit

**HTH** helix-turn-helix

LL long loop

**DCCM** dynamical cross correlation matrix

MI mutual information

**PCA** principal component analysis

#### REFERENCES

 Shabb JB. Physiological substrates of cAMP-dependent protein kinase. Chem. Rev. 2001; 101:2381–2411. [PubMed: 11749379]

- 2. Taylor SS, Yang J, Wu J, Haste NM, Radzio-Andzelm E, Anand G. PKA: a portrait of protein kinase dynamics. Biochim. Biophys. Acta. 2004; 1697:259–269. [PubMed: 15023366]
- 3. Zhang P, Smith-Nguyen EV, Keshwani MM, Deal MS, Kornev AP, Taylor SS. Structure and allostery of the PKA RIIbeta tetrameric holoenzyme. Science. 2012; 335:712–716. [PubMed: 22323819]
- 4. Boeshans KM, Resing KA, Hunt JB, Ahn NG, Shabb JB. Structural characterization of the membrane-associated regulatory subunit of type I cAMP-dependent protein kinase by mass spectrometry: Identification of Ser81 as the in vivo phosphorylation site of RI-alpha. Protein Sci. 1999; 8:1515–1522. [PubMed: 10422841]
- 5. Taylor SS, Kim C, Vigil D, Haste NM, Yang J, Wu J, Anand GS. Dynamics of signaling by PKA. Biochim. Biophys. Acta. 2005; 1754:25–37. [PubMed: 16214430]
- Knighton DR, Zheng JH, Ten Eyck LF, Ashford VA, Xuong NH, Taylor SS, Sowadski JM. Crystal structure of the catalytic subunit of cyclic adenosine monophosphate-dependent protein kinase. Science. 1991; 253:407–414. [PubMed: 1862342]
- Johnson DA, Akamine P, Radzio-Andzelm E, Madhusudan M, Taylor SS. Dynamics of cAMPdependent protein kinase. Chem. Rev. 2001; 101:2243–2270. [PubMed: 11749372]
- Masterson LR, Cheng C, Yu T, Tonelli M, Kornev AP, Taylor SS, Veglia G. Dynamics connect substrate recognition to catalysis in protein kinase A. Nat Chem Biol. 2010; 6:821–828. [PubMed: 20890288]
- Masterson LR, Cembran A, Shi L, Veglia G. Allostery and binding cooperativity of the catalytic subunit of protein kinase A by NMR spectroscopy and molecular dynamics simulations. Adv. Protein Chem. Struct. Biol. 2012; 87:363–389. [PubMed: 22607761]
- 10. Kornev AP, Taylor SS. Protein Kinases: Evolution of a Dynamic Regulatory Protein. Trends in biochemical sciences. 2010; 36:65–77. [PubMed: 20971646]
- Masterson LR, Shi L, Metcalfe E, Gao J, Taylor SS, Veglia G. Dynamically committed, uncommitted, and quenched states encoded in protein kinase A revealed by NMR spectroscopy. Proc. Natl. Acad. Sci. U. S. A. 2011; 108:6969–6974. [PubMed: 21471451]
- 12. Jedrzejewski PT, Girod A, Tholey A, König N, Thullner S, Kinzel V, Bossemeyer D. A conserved deamidation site at asn 2 in the catalytic subunit of mammalian cAMP-dependent protein kinase detected by capillary LC-MS and tandem mass spectrometry. Protein Science. 2008; 7:457–469. [PubMed: 9521123]
- Tholey A, Pipkorn R, Bossemeyer D, Kinzel V, Reed J. Influence of myristoylation, phosphorylation, and deamidation on the structural behavior of the N-terminus of the catalytic subunit of cAMP-dependent protein kinase. Biochemistry. 2001; 40:225–231. [PubMed: 11141074]
- 14. Yang J, Wu J, Steichen JM, Kornev AP, Deal MS, Li S, Sankaran B, Woods VL Jr, Taylor SS. A conserved Glu-Arg salt bridge connects coevolved motifs that define the eukaryotic protein kinase fold. J. Mol. Biol. 2012; 415:666–679. [PubMed: 22138346]
- Sastri M, Barraclough DM, Carmichael PT, Taylor SS. A-kinase-interacting protein localizes protein kinase A in the nucleus. Proc. Natl. Acad. Sci. U. S. A. 2005; 102:349–354. [PubMed: 15630084]
- Gangal M, Clifford T, Deich J, Chen X, Taylor SS, Johnson DA. Mobilization of the A-kinase N-myristate through an Isoform-specific Intermolecular Switch. Proc Natl Acad Sci USA. 1999; 96:12394–12399. [PubMed: 10535933]
- 17. Gaffarogullari EC, Masterson LR, Metcalfe EE, Traaseth NJ, Balatri E, Musa MM, Mullen D, Distefano MD, Veglia G. A Myristoyl/Phosphoserine Switch Controls cAMP-Dependent Protein Kinase Association to Membranes. J. Mol. Biol. 2011; 411:823–836. [PubMed: 21740913]
- Bastidas AC, Deal MS, Steichen JM, Keshwani MM, Guo Y, Taylor SS. Role of N-terminal Myristylation in the Structure and Regulation of cAMP-Dependent Protein Kinase. Journal of Molecular Biology. 2012; 422:215–229. [PubMed: 22617327]

19. Herberg FW, Zimmermann B, McGlone M, Taylor SS. Importance of the A-helix of the catalytic subunit of cAMP-dependent protein kinase for stability and for orienting subdomains at the cleft interface. Protein Sci. 1997; 6:569–579. [PubMed: 9070439]

- Veron M, Radzio-Andzelm E, Tsigelny I, Ten Eyck LF, Taylor SS. A conserved helix motif complements the protein kinase core. Proc. Natl. Acad. Sci. U. S. A. 1993; 90:10618–10622. [PubMed: 7504272]
- Zheng J, Knighton DR, Nguyen HX, Taylor SS, Sowadski JM, Ten Eyck LF. Crystal structures of the myristylated catalytic subunit of cAMP-dependent protein kinase reveal open and closed conformations. Protein Sci. 1993; 2:1559–1573. [PubMed: 8251932]
- 22. Zheng J, Trafny EA, Knighton DR, Xuong NH, Taylor SS, Ten Eyck LF, Sowadski JM. 2.2 A refined crystal structure of the catalytic subunit of cAMP-dependent protein kinase complexed with MnATP and a peptide inhibitor. Acta Crystallogr. D Biol. Crystallogr. 1993; 49:362–365. [PubMed: 15299527]
- Cox S, Taylor SS. Kinetic analysis of cAMP-dependent protein kinase: mutations at histidine 87
  affect peptide binding and pH dependence. Biochemistry. 1995; 34:16203–16209. [PubMed:
  8519778]
- 24. Cook PF, Neville ME, Vrana KE, Hartl FT, Roskoshi R. Adenosine Cyclic 3'5'-Monophosphate Dependent Protein Kinase: Kinetic Mechanism for the Bovine Skeletal Muscle Catalytic Subunit. Biochemistry. 1982; 21:5794–5799. [PubMed: 6295440]
- 25. Glass DB, Cheng HC, Mende-Mueller L, Reed J, Walsh DA. Primary structural determinants essential for potent inhibition of cAMP-dependent protein kinase by inhibitory peptides corresponding to the active portion of the heat-stable inhibitor protein. J. Biol. Chem. 1989; 264:8802–8810. [PubMed: 2722799]
- Jorgensen WL, Chandrasekhar J, Madura JD, Impey RW, Klein ML. Comparison of simple potential functions for simulating liquid water. J. Chem. Phys. 1983; 79:926–935.
- 27. MacKerell AD, Bashford D, Dunbrack RL, Evanseck JD, Field MJ, Fischer S, Gao J, Guo H, Ha S, Joseph-McCarthy D, Kuchnir L, Kuczera K, Lau FTK, Mattos C, Michnick S, Ngo T, Nguyen DT, Prodhom B, Reiher WE, Roux B, Schlenkrich M, Smith JC, Stote R, Straub J, Watanabe M, Wiórkiewicz-Kuczera J, Yin D, Karplus M. All-Atom Empirical Potential for Molecular Modeling and Dynamics Studies of Proteins †. The Journal of Physical Chemistry B. 1998; 102:3586–3616.
- Mackerell AD Jr, Feig M, Brooks CL 3rd. Extending the treatment of backbone energetics in protein force fields: limitations of gas-phase quantum mechanics in reproducing protein conformational distributions in molecular dynamics simulations. J. Comput. Chem. 2004; 25:1400–1415. [PubMed: 15185334]
- 29. MacKerell AD Jr, Banavali N, Foloppe N. Development and current status of the CHARMM force field for nucleic acids. Biopolymers. 2000; 56:257–265. [PubMed: 11754339]
- 30. Klauda JB, Venable RM, Freites JA, O'Connor JW, Tobias DJ, Mondragon-Ramirez C, Vorobyov I, MacKerell AD Jr, Pastor RW. Update of the CHARMM all-atom additive force field for lipids: validation on six lipid types. J Phys Chem B. 2010; 114:7830–7843. [PubMed: 20496934]
- 31. Brooks BR, Bruccoleri RE, Olafson BD, States DJ, Swaminathan S, Karplus M. CHARMM: a program for macromolecular energy, minimization, and dynamics calculations. Journal of Computational Chemistry. 1983; 4:187–217.
- 32. Brooks BR, Brooks CL 3rd, Mackerell AD Jr, Nilsson L, Petrella RJ, Roux B, Won Y, Archontis G, Bartels C, Boresch S, Caflisch A, Caves L, Cui Q, Dinner AR, Feig M, Fischer S, Gao J, Hodoscek M, Im W, Kuczera K, Lazaridis T, Ma J, Ovchinnikov V, Paci E, Pastor RW, Post CB, Pu JZ, Schaefer M, Tidor B, Venable RM, Woodcock HL, Wu X, Yang W, York DM, Karplus M. CHARMM: the biomolecular simulation program. J. Comput. Chem. 2009; 30:1545–1614. [PubMed: 19444816]
- 33. Phillips JC, Braun R, Wang W, Gumbart J, Tajkhorshid E, Villa E, Chipot C, Skeel RD, Kale L, Schulten K. Scalable molecular dynamics with NAMD. J. Comput. Chem. 2005; 26:1781–1802. [PubMed: 16222654]
- 34. Andersen HC. Rattle: A "velocity" version of the shake algorithm for molecular dynamics calculations. Journal of Computational Physics. 1983; 52:24–34.

35. Tuckerman M, Berne BJ, Martyna GJ. Reversible Multiple Time Scale Molecular-Dynamics. J Phys Chem B. 1992; 97:1990–2001.

- 36. Darden T, Perera L, Li L, Pedersen L. New tricks for modelers from the crystallography toolkit: the particle mesh Ewald algorithm and its use in nucleic acid simulations. Structure. 1999; 7:R55–60. [PubMed: 10368306]
- Martyna GJ, Tobias DJ, Klein ML. Constant-Pressure Molecular-Dynamics Algorithms. J Chem Phys. 1994; 101:4177–4189.
- 38. Amadei A, Linssen AB, Berendsen HJ. Essential dynamics of proteins. Proteins. 1993; 17:412–425. [PubMed: 8108382]
- Grant BJ, Rodrigues AP, ElSawy KM, McCammon JA, Caves LS. Bio3d: an R package for the comparative analysis of protein structures\. Bioinformatics. 2006; 22:2695–2696. [PubMed: 16940322]
- Jammalamadaka, SR.; SenGupta, A. Topics in Circular Statistics. World Scientific; River Edge, N.J: 2001. 2001
- 41. Li DW, Meng D, Bruschweiler R. Short-range coherence of internal protein dynamics revealed by high precision in silico study. J. Am. Chem. Soc. 2009; 131:14610–14611. [PubMed: 19780553]
- McClendon CL, Friedland G, Mobley DL, Amirkhani H, Jacobson MP. Quantifying Correlations Between Allosteric Sites in Thermodynamic Ensembles. J. Chem. Theory Comput. 2009; 5:2486–2502. [PubMed: 20161451]
- Killian BJ, Yundenfreund Kravitz J, Gilson MK. Extraction of configurational entropy from molecular simulations via an expansion approximation. J. Chem. Phys. 2007; 127:024107.
   [PubMed: 17640119]
- 44. Morcos F, Chatterjee S, McClendon CL, Brenner PR, Lopez-Rendon R, Zintsmaster J, Ercsey-Ravasz M, Sweet CR, Jacobson MP, Peng JW, Izaguirre JA. Modeling conformational ensembles of slow functional motions in Pin1-WW. PLoS Comput. Biol. 2010; 6:e1001015. [PubMed: 21152000]
- 45. Fatmi MQ, Chang CE. The role of oligomerization and cooperative regulation in protein function: the case of tryptophan synthase. PLoS Comput. Biol. 2010; 6:e1000994. [PubMed: 21085641]
- 46. Masterson LR, Shi L, Tonelli M, Mascioni A, Mueller MM, Veglia G. Backbone NMR resonance assignment of the catalytic subunit of cAMP-dependent protein kinase A in complex with AMP-PNP. Biomol. NMR Assign. 2009; 3:115–117. [PubMed: 19636960]
- 47. Yonemoto W, McGlone ML, Taylor SS. N-myristylation of the catalytic subunit of cAMP-dependent protein kinase conveys structural stability. J. Biol. Chem. 1993; 268:2348–2352. [PubMed: 8428909]
- 48. Zheng J, Knighton DR, ten Eyck LF, Karlsson R, Xuong N, Taylor SS, Sowadski JM. Crystal structure of the catalytic subunit of cAMP-dependent protein kinase complexed with MgATP and peptide inhibitor. Biochemistry. 1993; 32:2154–2161. [PubMed: 8443157]
- 49. Minoux H, Chipot C. Cation-π Interactions in Proteins: Can Simple Models Provide an Accurate Description? J. Am. Chem. Soc. 1999; 121:10366–10372.
- Woolf TB, Grossfield A, Pearson JG. Indoles at interfaces: Calculations of electrostatic effects with density functional and molecular dynamics methods. International Journal of Quantum Chemistry. 1999; 75:197–206.
- 51. Gilis D, Biot C, Buisine E, Dehouck Y, Rooman M. Development of Novel Statistical Potentials Describing Cation- $\pi$  Interactions in Proteins and Comparison with Semiempirical and Quantum Chemistry Approaches. J. Chem. Inf. Model. 2006; 46:884–893. [PubMed: 16563020]
- 52. Kornev AP, Taylor SS. Defining the conserved internal architecture of a protein kinase. Biochim. Biophys. Acta. 2009; 1804:440–444. [PubMed: 19879387]
- 53. Watt ED, Rivalta I, Whittier SK, Batista VS, Loria JP. Reengineering rate-limiting, millisecond enzyme motions by introduction of an unnatural amino acid. Biophys. J. 2011; 101:411–420. [PubMed: 21767494]
- 54. Hammes-Schiffer S, Benkovic SJ. Relating protein motion to catalysis. Annu. Rev. Biochem. 2006; 75:519–541. [PubMed: 16756501]
- 55. Boehr DD, McElheny D, Dyson HJ, Wright PE. The dynamic energy landscape of dihydrofolate reductase catalysis. Science. 2006; 313:1638–1642. [PubMed: 16973882]

 Frederick KK, Marlow MS, Valentine KG, Wand AJ. Conformational entropy in molecular recognition by proteins. Nature. 2007; 448:325–329. [PubMed: 17637663]

- 57. Yao X, Rosen MK, Gardner KH. Estimation of the available free energy in a LOV2-J alpha photoswitch. Nat. Chem. Biol. 2008; 4:491–497. [PubMed: 18604202]
- 58. Gsponer J, Christodoulou J, Cavalli A, Bui JM, Richter B, Dobson CM, Vendruscolo M. A coupled equilibrium shift mechanism in calmodulin-mediated signal transduction. Structure. 2008; 16:736–746. [PubMed: 18462678]
- 59. Mittag T, Kay LE, Forman-Kay JD. Protein dynamics and conformational disorder in molecular recognition. J. Mol. Recognit. 2010; 23:105–116. [PubMed: 19585546]
- 60. Wright PE, Dyson HJ. Linking folding and binding. Curr. Opin. Struct. Biol. 2009; 19:31–38. [PubMed: 19157855]
- 61. Smock RG, Gierasch LM. Sending signals dynamically. Science. 2009; 324:198–203. [PubMed: 19359576]
- 62. Tzeng SR, Kalodimos CG. Dynamic activation of an allosteric regulatory protein. Nature. 2009; 462:368–372. [PubMed: 19924217]
- 63. Ma B, Nussinov R. Enzyme dynamics point to stepwise conformational selection in catalysis. Curr. Opin. Chem. Biol. 2010; 14:652–659. [PubMed: 20822947]
- 64. Cui Q, Karplus M. Allostery and cooperativity revisited. Protein Sci. 2008; 17:1295–1307. [PubMed: 18560010]
- 65. Popovych N, Sun S, Ebright RH, Kalodimos CG. Dynamically driven protein allostery. Nat. Struct. Mol. Biol. 2006; 13:831–838. [PubMed: 16906160]
- Cooper A, Dryden DT. Allostery without conformational change. A plausible model. Eur. Biophys. J. 1984: 11:103–109.
- 67. Clegg RA, Bowen LC, Bicknell AV, Tabish M, Prescott MC, Rees HH, Fisher MJ. Characterisation of the N'1 isoform of the cyclic AMP-dependent protein kinase (PK-A) catalytic subunit in the nematode, Caenorhabditis elegans. Arch. Biochem. Biophys. 2012; 519:38–45. [PubMed: 22286028]
- 68. Zhang J, Adrian FJ, Jahnke W, Cowan-Jacob SW, Li AG, Iacob RE, Sim T, Powers J, Dierks C, Sun F, Guo GR, Ding Q, Okram B, Choi Y, Wojciechowski A, Deng X, Liu G, Fendrich G, Strauss A, Vajpai N, Grzesiek S, Tuntland T, Liu Y, Bursulaya B, Azam M, Manley PW, Engen JR, Daley GQ, Warmuth M, Gray NS. Targeting Bcr-Abl by combining allosteric with ATP-binding-site inhibitors. Nature. 2010; 463:501–506. [PubMed: 20072125]

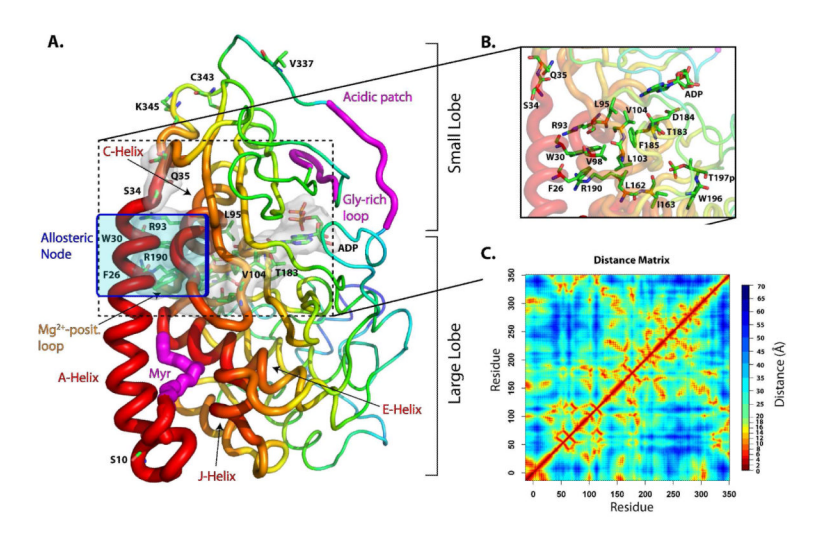


**Figure 1.**PKA-C structure summary. A) Relevant residues and regions discussed in the text are mapped on the structure of PKA-C. Regions in close contact with the A-helix and myristoyl group are highlighted with thicker ribbons and red colors. B) Close-up of the region at the interface between the two lobes, where most of the residues perturbed by myristoylation/S10-phosphorylation are located. C) Distance matrix for the myr(+)p(-)HTH simulation. Residues 1-350 correspond to the PKA-C amino acids, while the initial negative values refer to the myristoyl carbon atoms.

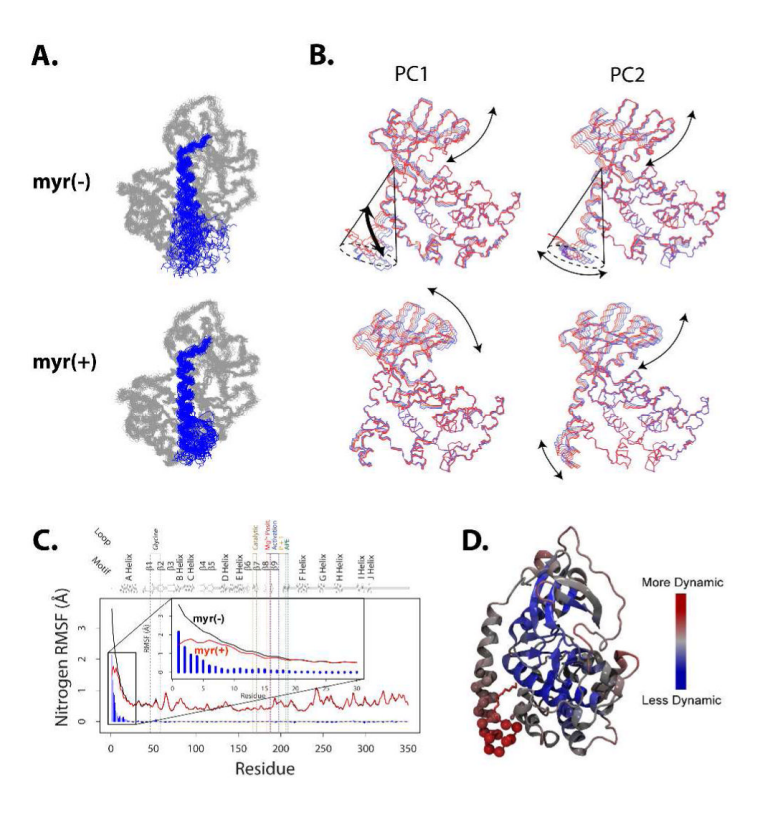


Figure 2. PKA-C Dynamics. A) Superposition of 33 snapshots of the myr(-)p(+) (top) and of the myr(+)p(+) simulations (bottom). B) First 2 PC for the myr(-)p(+) (top) and of the myr(+)p(+) simulations (bottom). C) - RMSF for backbone nitrogen. The myr(-)p(+) system is shown as a black line, and the myr(+)p(+) is shown in red. Blue bars show the difference in fluctuation "myr(-) - myr(+)". D) The myr(+) system RMSF is mapped onto the structure of PKA-C. Spheres highlight residues 1 to 20, which show the largest difference myr(-) - myr(+).

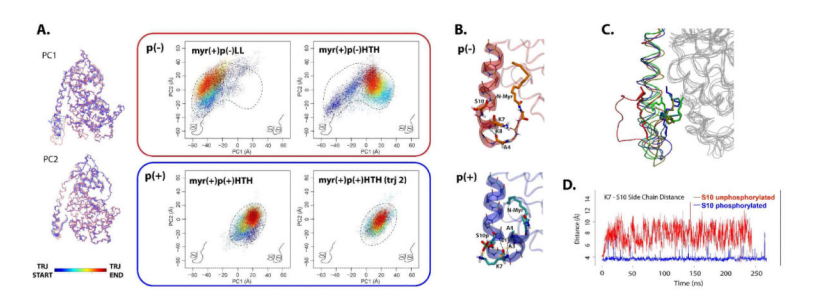


Figure 3.

LL/HTH conformational transition. A) PCA of the myr(+)p(-) and myr(+)p(+) trajectories pooled together for the kinase binary complex. The color gradient from blue to red tracks the trajectories' time evolution. PC1 separates the LL (left) and HTH (right) conformational basins. Dotted lines qualitatively show the conformational space accessible to the phosphporylated and un phosphorylated systems. B) Representative snapshots from the myr(+)p(-)LL simulations (top) and for the myr(+)p(+)HTH simulation (bottom). Dotted lines show hydrogen and ionic bonds. Yellow lines and arrow show the interactions that break and the angle that rotates in the LL/HTH transition. C) Five snapshots from the high-temperature trajectory, taken at progressively higher temperature from blue to green to red. D) Distance between the S10 hydroxyl oxygen and Lys-7 side-chain nitrogen for the myr(+)p(-)LL simulation (red) and between the S10 phosphate and Lys-7 side chain nitrogen for the myr(+)p(+)HTH simulation (blue).

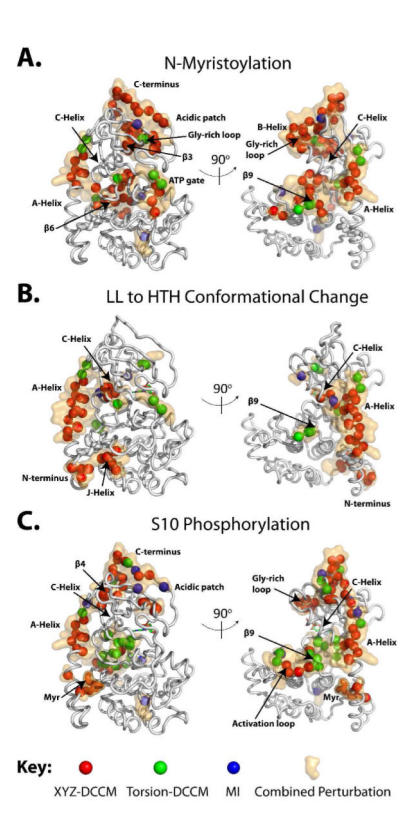


Figure 4. Allosteric Interaction map. Increased correlations/MI (see text) observed upon different perturbations are mapped on the kinase structure and color coded based on the method of discovery. A) Effects of N-myristoylation, as obtained by comparing the myr(+)p(+) and myr(-)p(+) simulations. B) Effects of LL to HTH conformational transition, as obtained by comparing the myr(+)p(-)LL and myr(+)p(-)HTH simulations. C) Effects of S10 phosphorylation, as obtained by comparing the myr(+)p(+) and myr(+)p(-)HTH simulations.

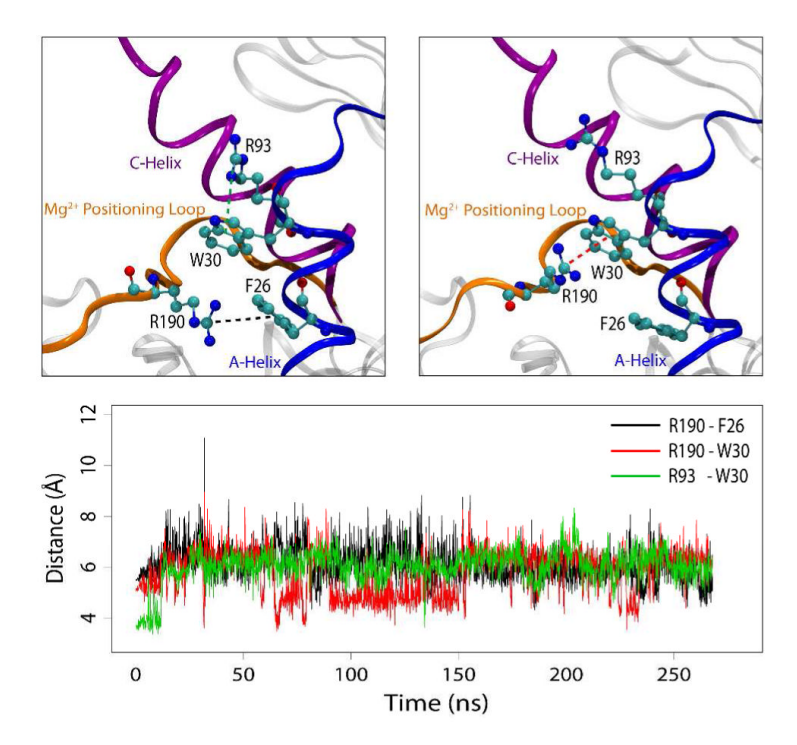
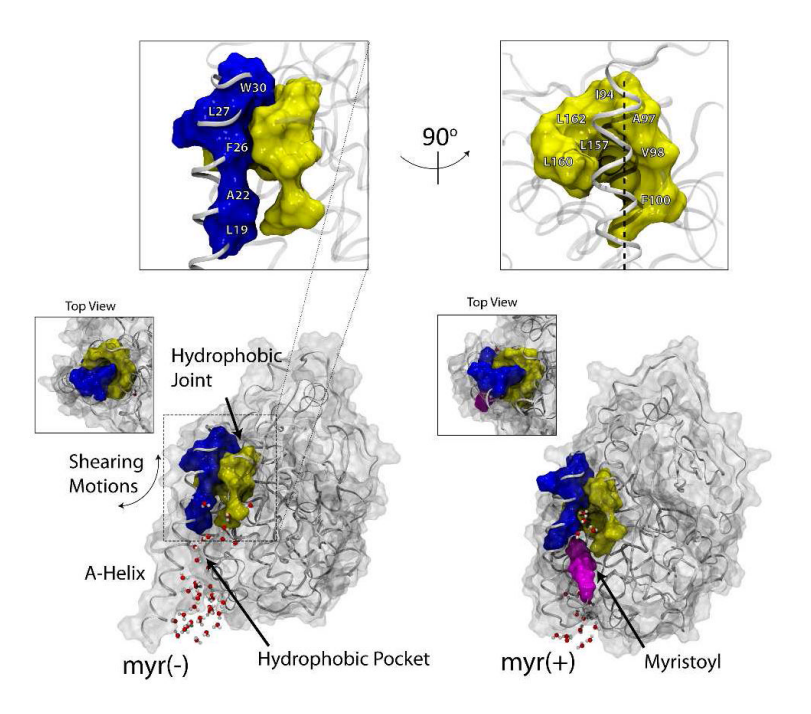


Figure 5. Cation- $\pi$  interactions. Details of the cation- $\pi$  interactions between F26/W30, R190, and R93. In the bottom panel, distances from the center of the rings to the center of the guanidinium moiety are shown for the myr(+)p(+) trajectory.



**Figure 6.** Hydrophobic joint and hydrophobic pocket. Top: close up view of the hydrophobic joint between A-helix and the apex of the loop between the C-helix and  $\beta 4$ , the E-helix and the C-terminal tail. The A-helix residues are highlighted on the left, and the ones forming the other face of the hydrophobic pocket are shown on the right, rotated by  $90^{\circ}$ . Bottom left: lateral view of the interface between the non-myristoylated PKA-C A-helix and the hydrophobic pocket. Water molecules in the hydrophobic pocket are shown with van der Waals spheres. Bottom right: lateral view of the myristoylated protein: almost all the waters in the hydrophobic pocked are displaced by the myristoyl group (shown in purple).

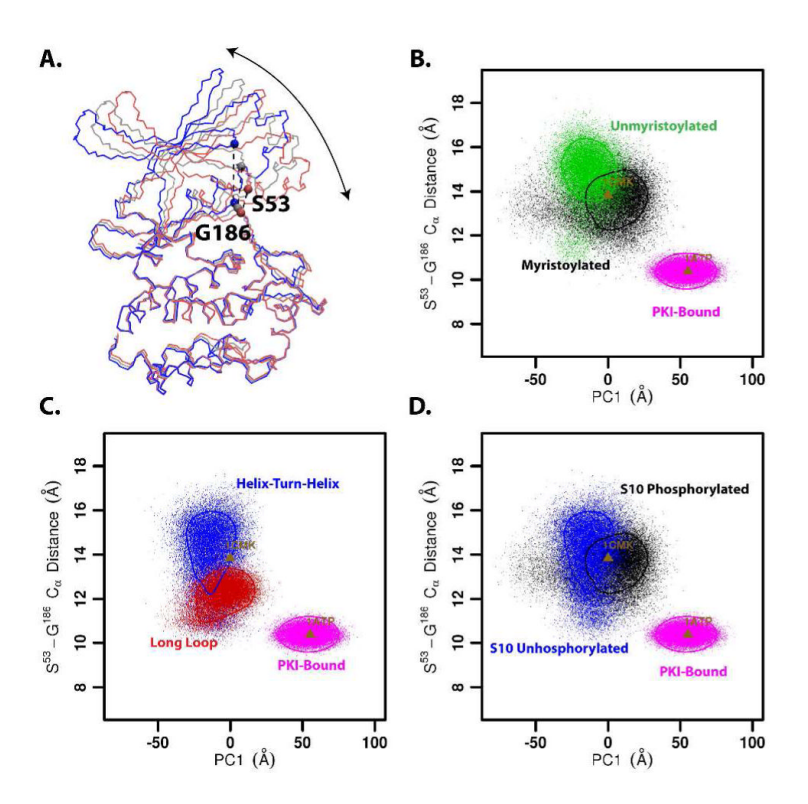


Figure 7. Opening/Closing modes. A) Lowest frequency principal component obtained by pooling all the trajectories together. Also shown are the  $C_{\alpha}$  carbons of S53 and G186, used to define the distance coordinate monitoring the opening/closing of the Gly-rich loop. B-D) Projection along PC1 and S53-G186 distance of the various trajectories.

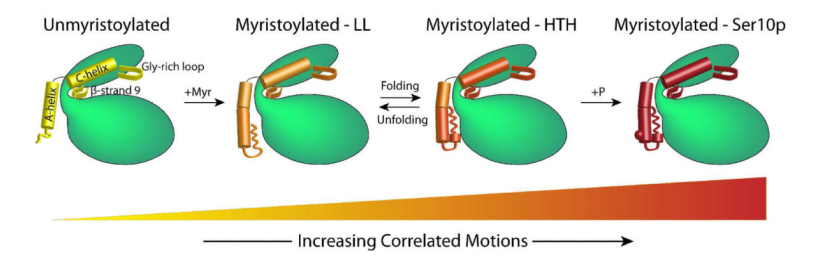


Figure 8. Allosteric Model. Increasing correlations between the N-terminus/A-helix and the  $\beta$ -strand 9/C-helix/Gly-rich loop are observed upon compaction of the kinase following myristoylation, LL to HTH transition, and S10 phosphorylation.